



Asteroseismology of KIC 11754974: a high-amplitude SX Phe pulsator in a 343-d binary system

S. J. Murphy,^{1,2*} A. Pigulski,³ D. W. Kurtz,¹ J. C. Suárez,⁴ G. Handler,⁵
 L. A. Balona,⁶ B. Smalley,⁷ K. Uytterhoeven,^{8,9} R. Szabó,¹⁰ A. O. Thygesen,^{11,12}
 V. Elkin,¹ M. Breger,^{13,14} A. Grigahcène,⁴ J. A. Guzik,¹⁵ J. M. Nemec¹⁶
 and J. Southworth⁷

¹Jeremiah Horrocks Institute, University of Central Lancashire, Preston PR1 2HE, UK

²Centro de Astrofísica, Faculdade de Ciências, Universidade do Porto, Rua das Estrelas, P-4150-762 Porto, Portugal

³Instytut Astronomiczny, Uniwersytet Wrocławski, Kopernika 11, PL-51-622 Wrocław, Poland

⁴Instituto de Astrofísica de Andalucía, Camino Bajo de Huétor 50, Granada E-18008, Spain

⁵Nicolaus Copernicus Astronomical Center, Bartycka 18, PL-00-716 Warsaw, Poland

⁶South African Astronomical Observatory, PO Box 9, Observatory 7935, Cape Town, South Africa

⁷Astrophysics Group, Keele University, Staffordshire ST5 5BG, UK

⁸Instituto de Astrofísica de Canarias, E-38200 La Laguna, Tenerife, Spain

⁹Department Astrofísica, Universidad de La Laguna, E-38206 La Laguna, Tenerife, Spain

¹⁰Konkoly Obs., Research Centre for Astronomy and Earth Sciences, HAS, H-1121 Budapest, Konkoly Thege Miklós út 15-17, Hungary

¹¹Zentrum Für Astronomie der Universität Heidelberg, Landessternwarte, Königstuhl 12, D-69117 Heidelberg, Germany

¹²Nordic Optical Telescope, Apartado 474, E-38700 Santa Cruz de La Palma, Santa Cruz de Tenerife, Spain

¹³Institut für Astronomie, Türkenschanzstraße 17, A-1180 Wien, Austria

¹⁴Department of Astronomy, University of Texas, Austin, TX 78712, USA

¹⁵Los Alamos National Laboratory, XTD-2 MS T-086, Los Alamos, NM 87545-2345, USA

¹⁶Department of Physics and Astronomy, Camosun College, Victoria, British Columbia V8P 5J2, Canada

Accepted 2013 April 4. Received 2013 April 3; in original form 2013 March 19

ABSTRACT

The candidate SX Phe star KIC 11754974 shows a remarkably high number of combination frequencies in the Fourier amplitude spectrum: 123 of the 166 frequencies in our multifrequency fit are linear combinations of independent modes. Predictable patterns in frequency spacings are seen in the Fourier transform of the light curve. We present an analysis of 180 d of short-cadence *Kepler* photometry and of new spectroscopic data for this evolved, late A-type star. We infer from the 1150-d, long-cadence light curve, and in two different ways, that our target is the primary of a 343-d, non-eclipsing binary system. According to both methods, the mass function is similar, $f(M) = 0.0207 \pm 0.0003 M_{\odot}$. The observed pulsations are modelled extensively, using separate, state-of-the-art, time-dependent convection (TDC) and rotating models. The models match the observed temperature and low metallicity, finding a mass of $1.50\text{--}1.56 M_{\odot}$. The models suggest that the whole star is metal poor, and that the low metallicity is not just a surface abundance peculiarity. This is the best frequency analysis of an SX Phe star, and the only *Kepler* δ Sct star to be modelled with both TDC and rotating models.

Key words: asteroseismology – stars: individual: KIC 11754974 – Stars: oscillations – stars: Population II – stars: variables: δ Scuti.

1 INTRODUCTION

The goal of the *Kepler* mission is to find Earth-like planets in the habitable zone (Koch et al. 2010). The methodology inherent in this task is the simultaneous, space-based observation of $\sim 150\,000$ stars in a $115\,\text{deg}^2$ field of view for transiting events.

Kepler observations are made in two cadences: most observations take place in long-cadence (LC) format, where photometric readouts are co-added for 29.4 min. Short-cadence (SC) observations have effective integration times of 58.8 s. These cadences make the data excellent for asteroseismic investigations. *Kepler* data are organized into quarters, denoted Q_n , and SC data are further subdivided into three one-month segments, denoted $Q_{n,m}$.

The success of the *Kepler* mission lies in its unprecedented μmag photometric precision. Even for a star as faint as KIC 11754974

*E-mail: smurphy6@uclan.ac.uk

($K_p = 12.7$ mag), the subject of this work, the average noise amplitude in the Fourier transform is $\sim 5 \mu\text{mag}$ at low frequency, decreasing gradually to $\sim 2 \mu\text{mag}$ for frequencies above about 70 d^{-1} .

Kepler photometry not only offers higher precision, but also provides nearly continuous observations. Progress in the analysis of δ Sct stars is no longer hampered by the insurmountable time gaps in the data associated with ground-based observations. Most stars now have almost continuous observations in LC mode from the commissioning run of Q0 right through to the most recent quarter at the time of writing (Q13), spanning over 1150 d; the same is true for some targets in SC mode. This long time-span is particularly important for resolving peaks that are very closely spaced in frequency, and for studies of frequency or amplitude modulation, among other reasons (see e.g. Murphy 2012b). Completely alleviating Nyquist ambiguities with *Kepler* data can now also be added to that list (Murphy, Shibahashi & Kurtz 2013).

The δ Sct stars are located at the junction of the classical Cepheid instability strip and the main sequence (MS), with pulsation periods between 18 min and 8 h. They are driven by the opacity mechanism in the He II partial ionization zone. SX Phe stars are the Population II counterparts of the δ Sct stars, characterized by low metallicity and high tangential velocities (Nemec & Mateo 1990; Balona & Nemec 2012). Within the last decade, observations of SX Phe stars have revealed that they are not necessarily intrinsically high-amplitude pulsators (Olech et al. 2005; Balona & Nemec 2012), but show amplitude distributions similar to the Population I δ Sct stars, viz., having peak pulsation amplitudes of a few mmag (see Uytterhoeven et al. 2011 for a statistical study). Traditionally, δ Sct stars with amplitudes above 0.3 mag were termed high-amplitude Delta Scuti (HADS) stars, and were found to pulsate mostly in one or two radial modes. Their high amplitudes are attributed to their evolved stages (e.g. Petersen & Christensen-Dalsgaard 1996, who describe HADS stars as being in the immediate post-MS stage). KIC 11754974 has a maximum peak-to-peak light variation of only 0.24 mag, based on tangential velocities was identified as an SX Phe star by Balona & Nemec (2012) and was the highest amplitude *Kepler* SX Phe star they identified. In this work, we find KIC 11754974 to have properties in common with both HADS and SX Phe stars.

2 BINARITY OF KIC 11754974

2.1 Doppler-shifted frequencies

Our target falls on *Kepler*'s failed Module 3, meaning it is only observed for three quarters of each year. For our frequency analysis, we utilized the higher sampling of the SC data, the longest uninterrupted run of which is Q6 and Q7, covering about 180 d. In the course of analysing the combined Q6+Q7 data set, it appeared that in Fourier spectra a significant residual signal occurs near the strongest terms after their subtraction. This indicated frequency and/or amplitude changes which prompted us to carry out the analysis separately for shorter data sets. Both LC and SC data were used in this analysis; they were split into 30–50 d subsets. For each subset, the frequency set containing the 72 strongest terms (20 independent and 52 harmonics and combinations) was fitted by means of non-linear least squares. The resulting frequencies of the strongest modes in different subsets were then compared. The result is shown in Fig. 1, where we plot the fractional frequency change of the four frequencies with the highest amplitudes in a given time subset, relative to their amplitudes in the arbitrarily chosen reference subset, here the SC Q6 data. As can be seen, the frequencies

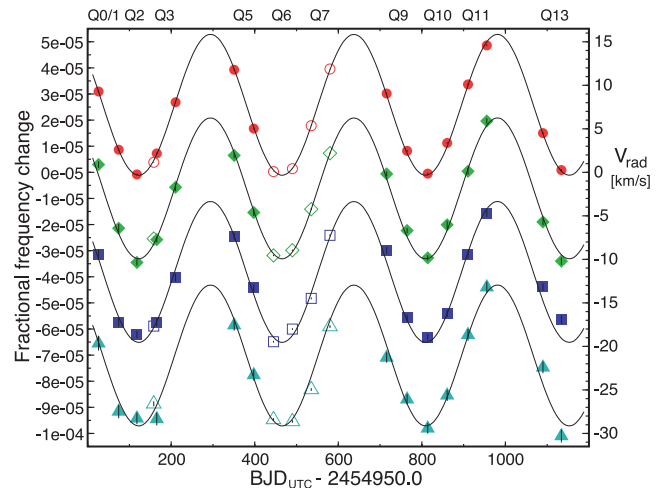


Figure 1. Temporal changes in the frequency of the four strongest modes excited in KIC 11754974, f_1, f_2, f_3 and f_4 , top to bottom. The values derived from LC and SC data are plotted with filled and open symbols, respectively. The sinusoid with a period of 343 d fitted to the f_1 data is also shown. For clarity, an offset has been added to the f_2, f_3 and f_4 data; the sinusoid has also been shifted accordingly. The right-hand side ordinate shows radial velocities calculated from the Doppler effect.

of all four of the strongest modes behave in the same manner and can be described by a sinusoid with a period of about 343 d.

The only plausible explanation of the changes seen in Fig. 1 is the motion of KIC 11754974 in a binary system. The frequency changes can be interpreted in terms of the Doppler effect and transformed to radial velocities via the equation

$$V_{\text{rad}} = c \frac{f_i - f_{\text{ref}}}{f_{\text{ref}}},$$

where c represents the speed of light. These radial velocities can be used to derive parameters of the spectroscopic orbit of the pulsating primary. It can be seen from Fig. 1 that the peak-to-peak radial velocity of KIC 11754974 amounts to about 16 km s^{-1} .

In order to derive parameters of the spectroscopic orbit, however, we proceeded in another way. Instead of using radial velocities calculated from frequencies, we decided to use the O – C diagram for the times of maximum light. The advantage of using the O – C diagram is that in this diagram the changes of period accumulate. For large orbital-to-pulsation period ratios, spectroscopic elements can be derived from the O – C diagram more accurately than when using radial velocities calculated from the Doppler effect.

Since the amplitude of the strongest mode is several times larger than the amplitudes of the next three modes, we decided to use only the times of maximum light of the strongest mode. First, all terms with amplitudes higher than 40 ppm except for f_1 and its harmonics were removed from the data. The residuals were divided into 5–20 d non-overlapping subsets. For each subset, a sinusoid with frequency f_1 and its harmonics were fitted in order to obtain amplitude and phase information. The time of maximum light was calculated from the phase of f_1 with the epoch adopted to be the nearest to the average time of observation in a given subset. The resulting observed (O) times of maximum light were compared to the calculated (C) times of maximum light according to the following ephemeris:

$$C(E) = 245\,4950.021\,179 + 0^d 061\,181\,7444 \times E,$$

where E is the number of cycles elapsed from the initial epoch, in BJD using Coordinated Universal Time (UTC; Eastman, Siverd &

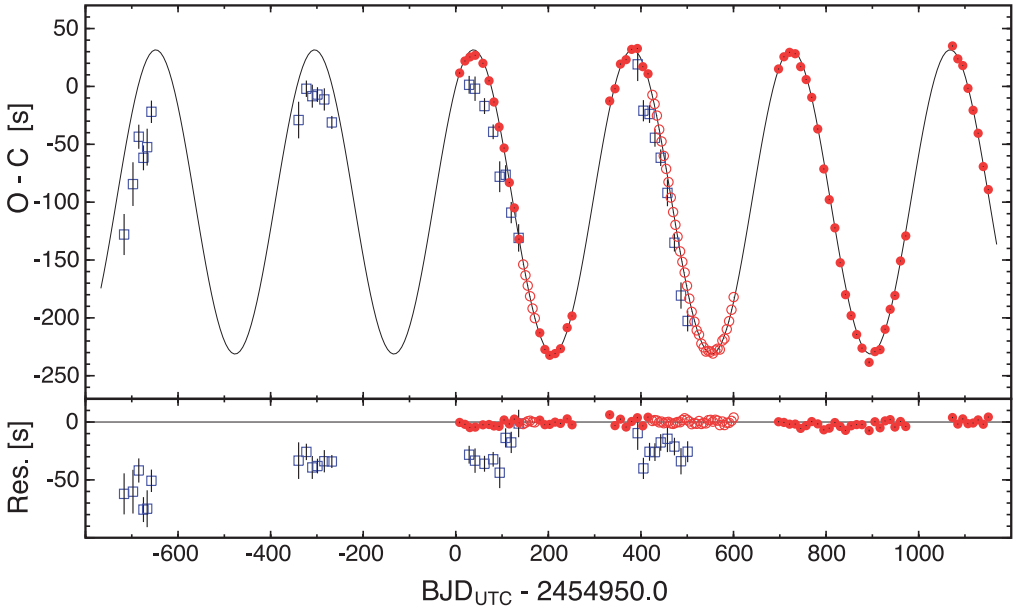


Figure 2. The O – C diagram for the times of maximum light of the strongest mode of KIC 11754974 (upper panel). The filled and open circles denote *Kepler* LC and SC data, respectively. The open squares represent the 2007–2010 WASP data. The lower panel shows the residuals from the eccentric orbit fit, shown as a continuous line in the upper panel. The parameters of the fit are given in Table 1.

Table 1. Parameters of the spectroscopic orbit derived from the O – C diagram. T_0 is given in BJD_{UTC}.

Parameter	Value
T_0	$2454\,999 \pm 37$
e	$0.013^{+0.011}_{-0.006}$
ω ($^\circ$)	102 ± 38
K_1 (km s^{-1})	8.35 ± 0.04
P_{orb} (d)	343.27 ± 0.34
P_0 (d)	$0.061\,181\,7444 \pm 0.000\,000\,0011$
$a_1 \sin i$ (au)	0.2634 ± 0.0013
$f(M)$ (M_\odot)	$0.020\,69 \pm 0.000\,31$

Gaudi 2010). As such, our *Kepler* times do not suffer the timing error discovered in 2012 November.¹

The Wide Angle Search for Planets (WASP) is a multisite, multicamera imaging system obtaining photometric data with an accuracy better than 1 per cent for objects with $7 \leq V \leq 11.5$ (Pollacco et al. 2006). Lower quality data are obtained for stars with $11.5 \leq V \leq 15$. Although the *Kepler* data have much higher precision and duty cycle, the WASP observations have time-spans extending back to years before *Kepler* came online. We utilized this longer time-base of the WASP data to confirm our O – C results, the values of which are plotted in Fig. 2.

Using the more precise *Kepler* times of maximum light (for both LC and SC data), we fitted the O – C parameters assuming an eccentric orbit. The parameters of the fit are given in Table 1. The meaning of the parameters is standard: T_0 denotes the epoch of periastron passage; e , eccentricity; ω , longitude of periastron; K_1 , half-range of the primary’s radial velocity variation; P_{orb} , the orbital period; P_0 , the pulsation period; a_1 , the semimajor axis of primary’s absolute orbit; and $f(M)$, the mass function. The residuals from the

fit are equal to 3.28 s for the LC and 1.47 s for the SC data. At least part of the residual scatter comes from the small-amplitude variation due to modes that were not subtracted from the data.

The lower panel of Fig. 2 indicates that the WASP data have large residuals (in time) when compared with the *Kepler* data. We tested whether the shift is intrinsic by comparing two stars in which such shifts were deemed to be unlikely – we chose two relatively bright, short-period W UMa stars, namely KIC 8554005 and KIC 9392683 (1SWASP J191805.45+444115.4 and 1SWASP J190413.72+455657.6, respectively). We investigated the strongest (second) harmonic in the Fourier transform of each star, and define a parameter $DT = T_{\text{max}}(\text{WASP}) - T_{\text{max}}(\text{Kepler})$, where T_{max} represents the time of maximum light closest to the mean epoch of a given data set. For KIC 8554005, we determine $DT = -5.8 \pm 5.2$ s and for KIC 9392683 $DT = -13.7 \pm 6.0$ s, and note that DT is therefore zero to within $1-2\sigma$. For KIC 11754974, we found $DT = -34.2 \pm 2.8$ s from all data or -27.2 ± 2.1 s if the first season is excluded. We therefore conclude that the shift for KIC 11754974 is intrinsic and probably occurs because the WASP and *Kepler* bands are different; the central wavelengths are ~ 550 nm for WASP and ~ 660 nm for *Kepler*. We note that WASP and *Kepler* use heliocentric and barycentric Julian date, respectively, and that contributes up to a couple of seconds to the offset.

One can see that the orbit has a small eccentricity. The secondary is likely to be a low-mass MS star. Assuming that the primary’s mass lies in the range $1.5-2.5 M_\odot$, we get $M_2 = 0.42-0.58 M_\odot$ for inclination $i = 90^\circ$ and $M_2 = 0.65-0.87 M_\odot$ for $i = 45^\circ$. This indicates a K- or early M-type secondary companion. Its contribution to the total flux is therefore not larger than a few per cent unless the inclination is very low. This reduces the possibility of detection of variability of the secondary if present at all.

Having calculated the orbital elements, we have corrected the BJD times for SC Q6 and Q7 data for the light-time effect in the binary system. Because in different quarters different detectors and apertures are used, it is expected that fluxes from different quarters are not directly comparable and need to be scaled. Using the

¹ http://archive.stsci.edu/kepler/timing_error.html

amplitudes of the strongest modes, we found that the amplitudes derived from Q7 data are larger by a factor of 1.0087 than those obtained from Q6 data. Therefore, the Q7 data were divided by this factor prior to combining. Subsequently, this high-duty cycle combined Q6+Q7 SC data set was subject of time series analysis (Section 4), where we have used only these adjacent SC quarters to avoid aliasing difficulties.

2.2 Frequency-modulated stars

The effect of the binary system on light arrival times is that of frequency modulation for the pulsation modes. Shibahashi & Kurtz (2012) showed how a frequency multiplet is induced around each pulsation mode as a result of the binarity. The frequency spacing can be used to infer P_{orb} , and the amplitudes and phases of the frequency multiplet give T_0 , e and $f(M)$, provided the data set is longer than P_{orb} . $f(M)$ is calculable using the ratio of the amplitudes of the first orbital sidelobes to those of the central pulsation frequency (Shibahashi & Kurtz 2012). We used this method to check our binary parameters, and we will show that the results we obtain using this method are entirely consistent with those derived from the O – C diagram. We applied this methodology to the *Kepler* LC Q0–13 data set, spanning 1153 d (3.36 orbits).

We started with the highest amplitude peak in the Q0–13 data set, which lies at 16.344745 d^{-1} with an amplitude of 51.79 mmag. We extracted this peak and its orbital sidelobes and applied non-linear least-squares fitting routines to improve the frequencies, amplitudes and phases. From the mean spacing of the multiplet, we derive $P_{\text{orb}} = 343.66 \pm 0.48 \text{ d}$, which is consistent with that derived via the O – C diagram. Given the slightly lower uncertainty on P_{orb} from the latter method, we used the (O – C)-calculated value of P_{orb} to force-fit the sidelobes to be exactly equally spaced. We chose the zero-point in time, such that the sidelobes have the same phase with respect to each other, but are $\pi/2$ out of phase with the central frequency, thus demonstrating the triplet is orbital in nature. Table 2 displays the results for this frequency and three others, each of which shows a frequency triplet split by the orbital frequency.

Table 2. A least-squares fit of the frequency triplets for the four highest amplitude modes. The sidelobes are fixed at frequencies of $\nu_{\text{osc}} \pm \nu_{\text{orb}}$. The zero-point in time, $t_0 = \text{BJD}_{\text{UTC}} 245\,553\,31.395\,90$, was chosen so that the sidelobes have equal phases and the difference in phase between the sidelobes and central peak is $\pi/2$. Column 4 thus shows that the difference in phases of the sidelobes with each other is zero within the errors, and Column 5 demonstrates that their phase difference from the central peak is $\pi/2$ within the errors. Column 6 contains the amplitude ratios of the sidelobes to the central frequency. Since these values are small compared to unity, they are approximately equal to α , the amplitude of the phase modulation. Column 7 shows the expected theoretical outcome that the ratio of α to the oscillation frequency is the same for all triplets. We note that for the first triplet, the amplitudes of the sidelobes are only equal at the 4σ level, and that the errors provided are overestimated because there are still many frequencies left in the data.

Frequency (d^{-1})	Amplitude (mmag)	Phase (rad)	$\phi_{+1} - \phi_{-1}$ (rad)	$\langle \phi_{+1} - \phi_{-1} \rangle - \phi_0$ (rad)	$\alpha = (A_{+1} + A_{-1})/A_0$	α/ν_{osc} ($\times 10^{-3} \text{ d}$)
16.341 823	3.964 ± 0.048	-1.6554 ± 0.0120				
16.344 745	51.792 ± 0.049	-0.0545 ± 0.0009	-0.011 ± 0.017	-1.606 ± 0.008	0.157 ± 0.003	9.58 ± 0.16
16.347 667	4.148 ± 0.048	-1.6663 ± 0.0115				
21.396 067	1.116 ± 0.048	0.9328 ± 0.0427				
21.398 989	11.046 ± 0.049	2.5642 ± 0.0044	0.012 ± 0.060	-1.626 ± 0.030	0.204 ± 0.012	9.54 ± 0.58
21.401 911	1.140 ± 0.048	0.9443 ± 0.0418				
20.904 493	0.766 ± 0.048	0.0139 ± 0.0623				
20.907 414	8.320 ± 0.049	1.6598 ± 0.0059	0.045 ± 0.086	-1.623 ± 0.043	0.189 ± 0.016	9.02 ± 0.78
20.910 336	0.803 ± 0.048	0.0589 ± 0.0595				
20.940 632	0.584 ± 0.048	2.1123 ± 0.0818				
20.943 554	5.890 ± 0.049	-2.5581 ± 0.0083	-0.003 ± 0.114	-1.614 ± 0.058	0.202 ± 0.023	9.62 ± 1.10
20.946 475	0.603 ± 0.048	2.1090 ± 0.0792				

The mass function is calculable as

$$f(m_1, m_2, \sin i) = \left(\frac{A_{+1} + A_{-1}}{A_0} \right)^3 \frac{P_{\text{osc}}^3}{P_{\text{orb}}^2} \frac{c^3}{2\pi G},$$

where the amplitudes of the central, higher and lower frequency components of the triplet are denoted A_0 , A_{+1} and A_{-1} , respectively; P_{osc} is the oscillation period; and all quantities are in SI units. Via this method we find $f(M) = 0.020\,69 \pm 0.000\,36 M_{\odot}$, which is exactly the value calculated via the O – C method. Equation (23) of Shibahashi & Kurtz (2012) allows one to calculate $a_1 \sin i$, too, as

$$a_1 \sin i = \frac{P_{\text{osc}}}{2\pi} \alpha c.$$

Application of this formula yields $a_1 \sin i = 0.2629 \pm 0.0051 \text{ au}$, in good agreement with the O – C value.

The fact that such information is discernible from the Fourier transform highlights the importance of having continuous long-term observations available for δ Sct stars, whose high-amplitude, high-frequency pulsations produce sidelobes with high signal-to-noise (S/N).

We also looked for eclipses in the SC data at the times when the stars are aligned to the line of sight. The possibility of finding such a shallow eclipse in the residuals of the light curve of a binary with this long a period, even when our multifrequency fit was subtracted, was very small. Although we did not find an eclipse, for such a wide system this provides only a slight constraint on the orbital inclination (an upper limit that is near 90°).

3 SPECTROSCOPIC OBSERVATIONS

We obtained three spectra of KIC 11754974 with the FIES spectrograph at the 2.5-m Nordic Optical telescope (NOT). The star is too faint for high-resolution observations with these facilities so to obtain spectra of a higher S/N we observed with medium resolution ($R = 25\,000$). Even still, observing conditions rendered the S/N ratio of the obtained spectra low – the S/N ratio of the averaged spectrum, estimated from the noise level of reduced 1D spectra, is

about 45 in the spectral region of H α and about 40 near H β . The difficulties in determining the right continuum level limit the accuracy of our determinations, which are provided to offer some constraints on fundamental parameters, rather than as definite determinations. We stress that higher resolution, higher S/N spectra are still needed.

The Balmer-line profiles are good indicators of effective temperature for A-type stars; thus, we have compared observed and synthetic profiles of the H α and H β lines. The synthetic calculations of Balmer profiles were done using the SYNTHE code by Piskunov (1992) and model atmospheres from Heiter et al. (2002) with solar metallicity (as determined by Anders & Grevesse 1989). The source of the spectral line list was the Vienna Atomic Line Database (VALD; Kupka et al. 1999). Later analysis of metal lines demonstrated metal deficiency with respect to solar abundances, so we switched to working with low-metallicity models ([M/H] = −0.5). For H α and H β , the best fits for observed and synthetic profiles were obtained for this metallicity model, yielding $T_{\text{eff}} = 7000$ and 6800 K, respectively. Considering possible errors in continuum determination of several per cent, we estimate from the Balmer lines that $T_{\text{eff}} = 7000 \pm 200$ K.

With our spectral material we cannot make reliable determinations of other parameters, namely $\log g$ and the microturbulence velocity v_{mic} . We calculated a number of synthetic spectra keeping T_{eff} and one other parameter fixed (thus permitting the third variable to change), to find the best fit of the metal lines. After several iterations, we accepted a model atmosphere with $T_{\text{eff}} = 7000$ K, $\log g = 3.6$ (cgs) and did calculations for microturbulence velocity resulting in $v_{\text{mic}} = 2 \text{ km s}^{-1}$. This $\log g$ value is only loosely constrained and we considered that the star shows HADS-star characteristics and is probably more evolved. However, the $\log g$ value obtained is lower than we expected, given that cool δ Sct stars tend to pulsate in low overtones (Breger & Bregman 1975), and a low-overtone mode at 16 d^{-1} (the frequency of our highest amplitude mode) implies an evolutionary status much closer to the zero-age main sequence (ZAMS). We compared the spectrum with the spectrum of δ Sct itself, taken from the Elodie archive (<http://atlas.obs-hp.fr/elodie/>). The shapes of the H β profiles are very similar in these stars. However, the spectrum of δ Sct is richer in metal lines.

The weak spectral lines in KIC 11754974 are lost in the noise. In the averaged spectrum, we identified lines of Fe I, Fe II, Ti II, Mg I, Mg II and some others. For identification, we calculated a synthetic spectrum using our best-fitting parameters. From several lines including Fe II $\lambda 5018.440$, Mg I $\lambda 5172.684$, Mg I $\lambda 5183.604$, we determined a projected rotational velocity: $v \sin i = 31 \pm 2 \text{ km s}^{-1}$. A more cautious interpretation, taking into account more lines (with a poorer overall fit) is $v \sin i = 25 \pm 7 \text{ km s}^{-1}$ – given the low S/N of our spectrum, we adopt the more cautious $v \sin i$ value.

Using several lines, we determined the abundances of iron: $\log N/N_{\text{tot}} = -5.8 \pm 0.3$ (while solar is -4.54),² and for magnesium: $\log N/N_{\text{tot}} = -5.9 \pm 0.3$ (solar is -4.46). We note that fitting H α and H β with [M/H] = −1.0 yielded negligible differences from the [M/H] = −0.5 models. Many other chemical elements in the spectra also show significant deficiencies but the lines are blended or below the detection threshold and cannot be tested. There is a problem in that many lines of Fe I that are not visible in the observed spectra appear in synthetic ones and require yet lower abundances for best fitting than we obtained from available lines, the latter mostly belonging to Fe II. One must decrease the effective temperature to reduce such a disequilibrium. At least one strong

Table 3. Atmospheric parameters determined from spectroscopy.

T_{eff} (K)	$\log g$ (cgs)	[Fe/H] (dex)	$v \sin i$ (km s $^{-1}$)	v_{mic} (km s $^{-1}$)
7000 ± 200	3.6 ± 0.3	$-0.5^{+0.2}_{-0.5}$	25 ± 7	2

available line of Fe I 4404.750 Å shows similar abundances to the Fe II lines. This problem needs higher quality spectra for further analysis. Strömgren photometry is desirable for independent determinations of T_{eff} and $\log g$ parameters. Our parameter determination from spectroscopy is given in Table 3.

With these restrictions in mind, verification of the low metallicity was provided by a semi-automated routine for 476 lines from the VALD data base in the 5000–5200 Å wavelength range. The best-fitting [M/H] value using χ^2 minimization was -0.58 dex, when the $\log g$ value was held at the determined value of 3.6. The [M/H] value is not the [Fe/H] value, but is close to it.

An independent check on our spectroscopic T_{eff} can be obtained from the InfraRed Flux Method (IRFM) (Blackwell & Shallis 1977). There is no sign of any interstellar Na D lines in the spectrum, so reddening is expected to be negligible. Broad-band APASS photometry from UCAC4 (Zacharias et al. 2012) and 2MASS were used to estimate the observed bolometric flux. The IRFM was then used to determine $T_{\text{eff}} = 7110 \pm 150$ K, which is consistent with the T_{eff} from the spectral analysis.

As another check, we also calculated a quartic polynomial fit in $(g' - r')$ colour to calculate a temperature of 7170 K, but the uncertainty on this value is large at about ± 250 K (Uytterhoeven et al. 2011).

We used the spectrum to discern the star's kinematics, finding a velocity shift of -300 km s^{-1} , in agreement with Balona & Nemec (2012). We expect that the 16 km s^{-1} radial velocity variations inferred from the light curve (cf. Fig. 1) would be detectable from spectroscopic observations that were suitably spaced in time.

Underabundances of Fe-peak elements by factors of 10–100 are characteristic of the λ Boo stars, which comprise only ∼2 per cent of objects in the δ Sct spectral region (Paunzen et al. 2002). If this star is determined through a full abundance analysis to be of the λ Boo class, it will be the most intensely photometrically studied λ Boo star to date – only eight spectroscopic binary systems with suspected λ Boo components are currently known (Paunzen et al. 2012). With our low-S/N spectrum, it is not possible to determine whether C, N and O are normal, as in the λ Boo stars, but many elements seem underabundant with respect to the Sun. The observed abundances are entirely consistent with the classification of KIC 11754974 as an SX Phe star by Balona & Nemec (2012).

4 PULSATION CHARACTERIZATION

4.1 The data and preliminaries

In this paper, we analysed the SC Q6+Q7 light curves from the Kepler Asteroseismic Science Operations Center³ for the HADS star KIC 11754974, to which we make corrections to the times to account for the light-time effects associated with being in a binary system as mentioned in Section 2. We used the pre-search data conditioned data of the least-squares pipeline (PDC-LS), but made

² as indicated in logarithmic form in the VALD.

³ <http://kasoc.phys.au.dk>

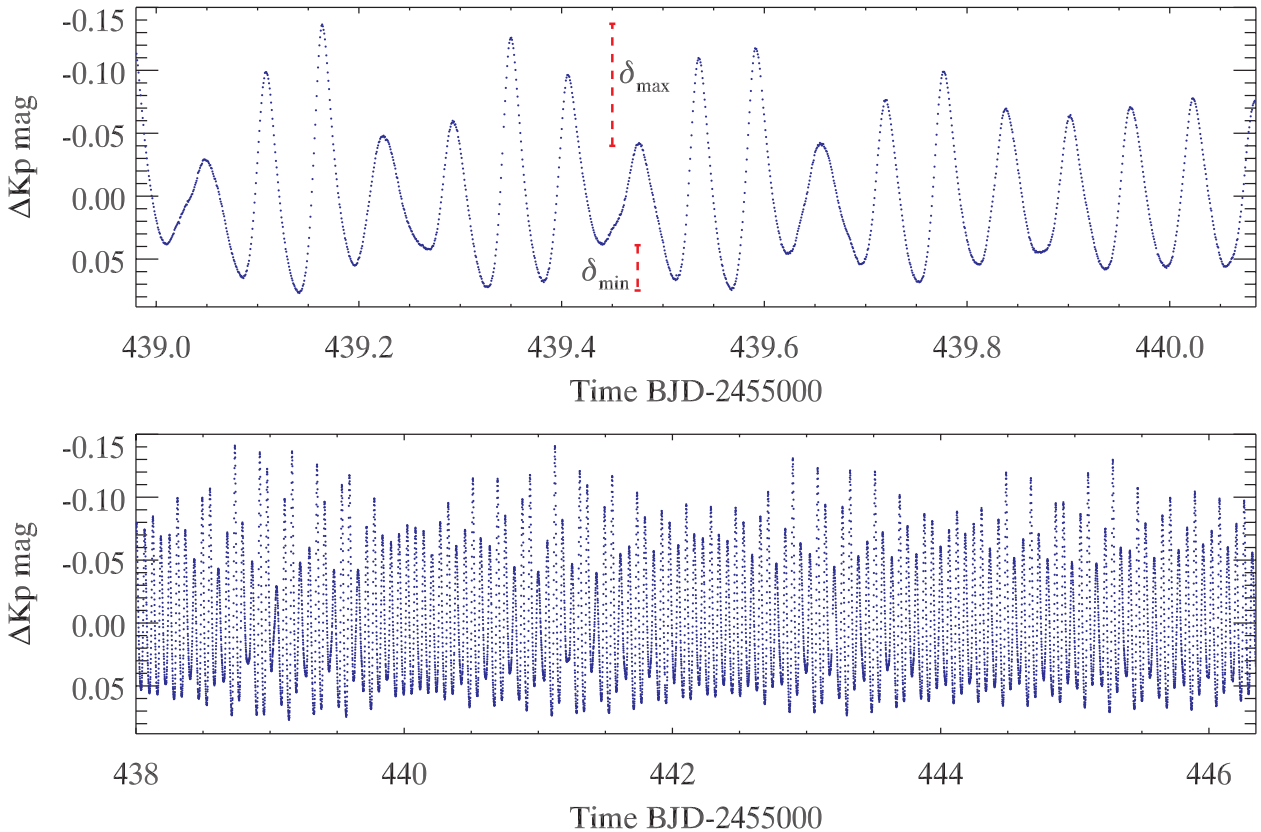


Figure 3. 1.1-d segment of the light curve of KIC 11754974, showing obvious beating. Flux maximum occurs over a greater range in brightness than does flux minimum, as indicated by the fact that $\delta_{\max} > \delta_{\min}$. The lower panel indicates this is not just localized to a short time segment.

checks with the Simple Aperture Photometry (SAP) data on which only basic calibration is performed in the data processing pipeline.

The PDC data are useful for their satisfactory removal of instrumental signals, including, but not limited to heating/cooling surrounding safe-mode events, cosmic ray events, and return to scientific operating focus and temperature after monthly downlinks (Kepler Data Characteristics Handbook⁴). The PDC data do not necessarily treat all jumps and outliers. For KIC 11754974, a manual check prior to analysis showed no clear outliers in need of removal; after fitting 166 frequencies, 103 ‘outliers’ of the 256 514 data points were manually discarded, 100 of which were at least 1 mmag from the fit, and the independent frequencies were thereafter improved with non-linear least-squares fitting. While in a limited number of cases the PDC data modify some stellar variability, known cases are documented in the data release notes available on the Kepler Guest Observer website,⁵ and the benefits of using PDC data over SAP data outweigh the detriments in this case. Further discussion on the implications to asteroseismology of choosing which of the SAP or PDC data to use can be found in Murphy (2012a,b).

We also note that the variability of KIC 11754974 was already discovered from the All Sky Automated Survey observations (Pigulski et al. 2009, star #143 in the catalogue). Due to the quality of the data, only the main mode was detected; we did not use those data in this investigation.

The data were imported into PERIOD04, for its useful graphical user interface, convenient least squares and discrete Fourier transform

functions, and tools for frequency extraction with pre-whitening. A review of the functions of PERIOD04 has been published by the program’s creators (Lenz & Breger 2004), and a more comprehensive view of its capabilities can be found in the user guide (Lenz & Breger 2005).

The corrected, edited Q6.1–Q7.3 data set contains 256 411 points taken from (BJD) 245 5372.439 to 245 5552.558 (180.12 d), having a 97 per cent duty cycle.

4.2 The light curve

We extracted 166 frequencies that are an excellent fit to the light curve. We recalculated our fit both after outlier extraction, and after removing a cubic spline fit. The latter was done by calculating the average residuals at 2-d intervals, interpolating with a cubic spline, and subtracting the smoothed curve from the original data. Semiregular cycles (Fig. 3, lower panel) are evident on different time-scales as a result of beating between frequencies.

The peaks in brightness occur over a greater intensity range than the troughs (Fig. 3, upper panel). This kind of light-curve shape is typical for HADS stars and can be thought of as saturation of the driving mechanism (Balona et al. 2011). It has also been observed in many γ Dor stars, and is common in RRab (RR Lyrae) variables. In particular, it is common in white dwarfs that show many combination frequencies in their pulsation spectra. Wu (2001) described how in white dwarfs, which pulsate in g modes, the convection turnover time is inferred from the phase of a combination frequency relative to its parents, and how the amplitude difference between the sums and differences in combination terms (e.g. $f_1 + f_2$ and $f_1 - f_2$) can

⁴ http://archive.stsci.edu/kepler/manuals/Data_Characteristics.pdf

⁵ <http://keplergo.arc.nasa.gov/Documentation.shtml>

give the thermal constant of the stellar convection zone at equilibrium. However, in an investigation into combination frequencies in δ Sct stars, Balona (2012) concluded that there is no information in the relative amplitude of a combination frequency that might be useful for mode identification in these p-mode pulsators.

4.3 The region of independent frequencies

In KIC 11754974, all of the high-amplitude independent frequencies are found in the range $16\text{--}25\text{ d}^{-1}$ (a full list of extracted frequencies with their corresponding amplitudes, along with identifications, is given in Table 4). Outside of this range, most frequencies detected can be explained as combination of dominant frequencies in the independently excited region. Such is also the case for the star 44 Tau, on which the literature is extensive. In KIC 11754974, independent peaks outside the $16\text{--}25\text{ d}^{-1}$ range have low amplitudes, typically of the order of $200\text{ }\mu\text{mag}$.

In HADS stars, the period ratio of the two most dominant modes offers easy mode identification when that ratio is 0.77 (Poretti 2003, for example), as this is the theoretical period ratio of the first radial overtone mode (hereafter $F1$) to the fundamental radial mode ($F0$). The period ratio can be plotted against the base-10 logarithm of the period of $F0$, $\log P(F0)$, in a so-called Petersen diagram,⁶ offering diagnostic information on the star. Petersen & Christensen-Dalsgaard (1996) discuss the diagrams in detail for double-mode HADS stars of different metallicities in their fig. 3. They showed that lower values of the $P(F1)/P(F1)$ ratio are found for metal-rich stars and stars closer to the ZAMS, but spectroscopy of KIC 11754974 indicates that this star has neither property. Hence, the period ratio of its two highest amplitude modes, f_1 and f_2 , having $P(f_2)/P(f_1) = 0.7638$, is much below the anticipated value (>0.770) from the metallicity-calibrated Petersen diagrams. We can thus argue that f_1 and f_2 are not the $F1$ and $F1$ modes. We also note that the high-amplitude independent frequencies around 21 d^{-1} (Figs 4 and 5), particularly f_3 and f_4 , could each potentially be the first radial overtone based on period ratios, though not all can be $\ell = 0$ modes, and none exactly gives the anticipated ratio.

The high amplitude of f_1 alone does not necessarily imply it is the fundamental radial mode, either; in FG Vir whose pulsation amplitudes are comparable to this star, the fundamental radial mode was not found to be the highest in amplitude of the observed frequencies (Guzik, Bradley & Templeton 2000; Breger et al. 2005). 4 CVn is another example (Breger, Davis & Dukes 2008; Castanheira et al. 2008). The high amplitude of f_1 does have other consequences: its window pattern dominates the entire analysed spectrum, even far from its frequency of 16.345 d^{-1} . Peaks arising solely from the spectral window of f_1 have amplitudes of 0.9 and 0.5 mmag at 50 and 100 d^{-1} , respectively. To make other peaks with lower amplitudes visible, Fig. 4 shows a schematic amplitude spectrum with all window patterns removed. The five highest amplitude peaks in the range $16\text{--}25\text{ d}^{-1}$ are all independent modes (note that the third and fourth highest peaks in that range are indistinguishable in Fig. 4). Other peaks with high amplitudes found outside this region are combinations of these frequencies.

Only once the five main independent modes are removed is it possible to see the high-frequency density in the Fourier transform.

⁶ The diagrams were first discussed by Petersen (1978), but it was Art N. Cox who brought the term ‘Petersen diagram’ into general use through his conference talks and eventually in his papers.

Fig. 5 allows a clearer view of the lower amplitude peaks surrounding the main pulsation frequencies. In this frequency range, independent frequencies are common, and few frequencies appear to be combinations. The spacing of 0.036 d^{-1} between f_3 and f_4 is found repeated in combination frequencies all over the spectrum, with different coefficients of f_1 and f_2 added to them.

4.4 Quintuplet

The Fourier transform of the light curve of the star features a quintuplet, with a central frequency at 20.242 d^{-1} , and two lower amplitude companions on each side with a mean separation of 0.218 d^{-1} , shown in Fig. 6 (upper panel). We assume that the quintuplet is rotationally split. The exact morphology of the quintuplet depends on excitation and orientation, but unless one can safely assume that components are excited to the same amplitude, the amplitude ratios cannot be used to constrain the star’s inclination. The separations are not perfectly identical between components, nor do we expect them to be for rotationally split quintuplets – exact frequency spacing is not expected unless there is frequency locking due to resonance (Buchler, Goupil & Hansen 1997). The need for high-dispersion spectroscopy or multicolour photometry is highlighted in this mode identification attempt – better spectroscopy can more tightly constrain both $v \sin i$ and the fundamental parameters required to improve the models (described in Section 5), allowing more certain mode identification.

In other case studies, peaks due to rotation have been found at low frequency with highly significant amplitudes (e.g. KIC 9700322; Breger et al. 2011; Guzik & Breger 2011). Hence, we searched the Q6 and Q7 SC data for a peak at low frequency that might correspond to the rotation frequency. There is no evidence for a peak at the anticipated value, nor at half or double that value (cf. Balona 2011). In fact, there is no evidence for a peak due to rotation below $\sim 0.8\text{ d}^{-1}$, which has implications for our modelling discussion Section 5.3. To check that such a peak was not somehow removed by either our spline fit or the PDC pipeline, the SAP data were also searched for the same peak, but no peak was found.

Another quintuplet occurs at $\sim 36.59\text{ d}^{-1}$ (Fig. 6, lower panel), but this is a manifestation of the main quintuplet in combination with f_1 . This is confirmed by inspecting the amplitudes of this second multiplet in light of the first – not only are they smaller, but they retain similar amplitude ratios between peaks within the multiplet. Similar quintuplets can be identified at 3.90 d^{-1} , arising from $f_{\text{quintuplet}} - f_1$, and at 12.45 d^{-1} from $2f_1 - f_{\text{quintuplet}}$. The frequency distribution and the amplitudes of the quintuplets are shown in Fig. 7.

4.5 Combination frequencies

The frequencies in Table 4 have been extracted down to an amplitude level of $100\text{ }\mu\text{mag}$ for the region $0\text{--}70\text{ d}^{-1}$, and to $20\text{ }\mu\text{mag}$ for $70\text{--}100\text{ d}^{-1}$ for closer examination of patterns. The region $70\text{--}100\text{ d}^{-1}$ shows the amplitude level at which pulsation-mode candidates can be identified. *Kepler* SC data allow high-frequency analysis, and the high precision of the satellite’s photometry, along with its position outside of Earth’s atmosphere, afford low noise levels ($<5\text{ }\mu\text{mag}$ for the region $70\text{--}100\text{ d}^{-1}$). The combination of the two make the detection of high-order frequency combinations possible.

The tolerance criterion for each calculated combination frequency has been chosen as 0.001 d^{-1} ; to be identified as a combination, the calculated frequency must agree with the observed frequency within this value. This tolerance is strict by some definitions – for the data set analysed, $1/T = 0.0056\text{ d}^{-1}$ and the full

Table 4. Multifrequency extraction and identification for KIC 11754972. The absence of combinations between 16 and 25 d⁻¹ is evident; the quintuplet and f_1-f_5 all lie in this region. Frequencies are only given an individual identification if they are of particular significance or form a combination. Errors on frequencies are generally smaller than 2×10^{-4} d⁻¹, and errors on amplitudes are all under 4 μmag . For f_1-f_5 , from which combinations are calculated, the frequency uncertainty is 10⁻⁶ d⁻¹.

Frequency (d ⁻¹)	Amplitude (μmag)	ID	Frequency (d ⁻¹)	Amplitude (μmag)	ID	Frequency (d ⁻¹)	Amplitude (μmag)	ID
16.344 74	633 29	f_1						
21.398 98	159 40	f_2						
20.907 40	116 53	f_3						
20.943 55	8229	f_4						
22.660 20	2839	f_5						
0.4554	270	$=f_2 - f_4$	20.4552	603	$=f_{11}^*$	42.7980	946	$=2f_2$
0.4916	865	$=f_2 - f_3$	20.6552	422	$=f_{12}^*$	43.5676	122	$=f_3 + f_5$
0.7723	202	$=f_7 - f_1$	21.0537	216		44.0592	389	$=f_2 + f_5$
1.0705	315	$=f_1 - f_6$	21.3973	257	†	44.4716	107	$=4f_1 - f_3$
1.2612	619	$=f_5 - f_2$	21.4282	274		47.8522	103	$=3f_2 - f_1$
1.3804	178	$=f_2 - f_9$	21.7251	458	$=f_{14}$	49.0342	2677	$=3f_1$
1.7528	250	$=f_5 - f_3$	22.5325	270		53.5969	1230	$=2f_1 + f_3$
3.4387	202	$=f_8 - f_1$	22.8592	107		53.6330	828	$=2f_1 + f_4$
3.6738	291	$=f_9 - f_1$	22.8860	205		54.0885	1466	$=2f_1 + f_2$
3.8976	334	$=f_{10} - f_1$	23.7744	354	$=f_{15}$	55.3497	235	$=2f_1 + f_5$
4.1040	141	$=f_{13} - f_1$	24.3270	130		58.1595	246	$=f_1 + 2f_3$
4.1105	161	$=f_{11} - f_1$	25.4701	257	$=2f_3 - f_1$	58.1957	174	$=f_1 + f_3 + f_4$
4.3108	76	$=f_{12} - f_1$	25.5062	229	$=f_3 + f_4 - f_1$	58.6511	292	$=f_1 + f_2 + f_3$
4.5627	4625	$=f_3 - f_1$	25.6208	242		58.6873	191	$=f_1 + f_2 + f_4$
4.5988	2234	$=f_4 - f_1$	25.9616	403	$=f_2 + f_3 - f_1$	59.1427	705	$=2f_2 + f_1$
5.0542	4435	$=f_2 - f_1$	25.9961	280		60.4039	165	$=f_1 + f_2 + f_5$
5.3804	119	$=f_{14} - f_1$	26.2959	441	$=f_{16}$	63.7054	152	$=2f_2 + f_3$
5.5458	118	$=2f_2 - f_1 - f_3$	26.4532	524	$=2f_2 - f_1$	63.7415	126	$=2f_2 + f_4$
6.2363	139	$=3f_1 - 2f_2$	26.5422	148		64.1969	292	$=3f_2$
6.3155	678	$=f_5 - f_1$	27.2590	105	$=f_4 + f_5 - f_1$	65.3790	628	$=4f_1$
6.7278	108	$=3f_1 - f_2 - f_3$	27.6352	481	$=3f_1 - f_2$	69.9416	418	$=3f_1 + f_3$
9.1253	116	$=2f_3 - 2f_1$	27.7144	172	$=f_2 + f_5 - f_1$	69.9778	241	$=3f_1 + f_4$
9.1615	112	$=f_3 + f_4 - 2f_1$	28.0907	238	$=3f_1 - f_4$	70.4332	318	$=3f_1 + f_2$
9.6169	204	$=f_2 + f_3 - 2f_1$	28.1268	426	$=3f_1 - f_3$	71.6944	70	$=3f_1 + f_5$
10.0293	361	$=2f_1 - f_5$	29.6549	393		74.5043	94	$=2f_1 + 2f_3$
10.1085	233	$=2f_2 - 2f_1$	29.6621	158		74.5404	132	$=2f_1 + f_3 + f_4$
11.2905	2066	$=2f_1 - f_2$	30.5486	112	$=2f_6$	74.9959	201	$=2f_1 + f_2 + f_3$
11.7459	1068	$=2f_1 - f_4$	31.6190	196	$=f_1 + f_6$	75.0320	79	$=2f_1 + f_2 + f_4$
11.7821	1844	$=2f_1 - f_3$	32.1979	141	$=2f_1 + f_3 - f_2$	75.4874	271	$=2f_1 + 2f_2$
12.0343	41	$=2f_1 - f_{12}$	32.6895	12 311	$=2f_1$	76.7487	67	$=2f_1 + f_2 + f_5$
12.2342	62	$=2f_1 - f_{11}$	32.7252	112	$=2f_1 + f_4 - f_3$	80.0501	99	$=2f_2 + f_1 + f_3$
12.4471	121	$=2f_1 - f_{10}$	33.1811	148	$=2f_1 + f_2 - f_3$	80.0863	110	$=f_1 + 2f_2 + f_4$
12.6709	107	$=2f_1 - f_9$	33.4618	272	$=f_1 + f_7$	80.5417	142	$=3f_2 + f_1$
12.9060	81	$=2f_1 - f_8$	36.1282	175	$=f_1 + f_8$	81.7237	182	$=5f_1$
14.5919	108	$=f_1 + f_3 - f_5$	36.3633	216	$=f_1 + f_9$	81.8029	41	$=f_1 + 2f_2 + f_5$
15.0835	262	$=f_1 + f_2 - f_5$	36.5871	270	$=f_1 + f_{10}$	85.5959	68	$=4f_2$
15.2743	692	$=f_6$	36.7935	112	$=f_1 + f_{13}$	86.2864	146	$=4f_1 + f_3$
15.8532	425	$=f_1 + f_3 - f_2$	36.8000	136	$=f_1 + f_{11}$	86.3225	77	$=4f_1 + f_4$
15.8893	180	$=f_1 + f_4 - f_2$	37.0000	74	$=f_1 + f_{12}$	86.7780	134	$=4f_1 + f_2$
16.3086	230	$=f_1 + f_3 - f_4$	37.2410	192		88.0392	29	$=4f_1 + f_5$
16.3618	155		37.2521	4143	$=f_1 + f_3$	90.8490	46	$=3f_1 + 2f_3$
16.3807	285	$=f_1 + f_4 - f_3$	37.2883	3158	$=f_1 + f_4$	90.8852	83	$=3f_1 + f_3 + f_4$
16.7999	141	$=f_1 + f_2 - f_4$	37.7437	5730	$=f_1 + f_2$	91.3406	120	$=3f_1 + f_2 + f_3$
16.8363	369	$=f_1 + f_2 - f_3$	37.9345	183	$=f_5 + f_6$	91.3768	32	$=3f_1 + f_2 + f_4$
17.1170	871	$=f_7$	38.0698	170	$=f_1 + f_{14}$	91.8322	97	$=3f_1 + 2f_2$
17.6060	212	$=f_1 + f_5 - f_2$	39.0049	795	$=f_1 + f_5$	93.0934	38	$=3f_1 + f_2 + f_5$
19.3224	424		40.1192	146	$=f_1 + f_{15}$	95.9033	32	$=2f_1 + f_2 + 2f_3$
19.7078	341		40.6909	295	$=f_3 + f_8$	95.9394	28	$=2f_1 + f_2 + f_3 + f_4$
19.7835	636	$=f_8^*$	41.4176	128	$=f_2 + f_9$	96.3949	91	$=2f_2 + 2f_1 + f_3$
19.8051	152		41.8148	494	$=2f_3$	96.4310	42	$=2f_1 + 2f_2 + f_4$
20.0186	814	$=f_9^*$	41.8509	760	$=f_4 + f_3$	96.8864	68	$=3f_2 + 2f_1$
20.2424	959	$=f_{10}^*$	42.3064	1139	$=f_2 + f_3$	98.0685	57	$=6f_1$
20.2487	126		42.3427	233	$=f_2 + f_4$	98.1476	27	$=2f_1 + 2f_2 + f_5$
20.4487	508	$=f_{13}$	42.6408	103	$=f_1 + f_{16}$			

* denotes quintuplet membership. † – this frequency is not fully resolved from f_2 in the SC data.

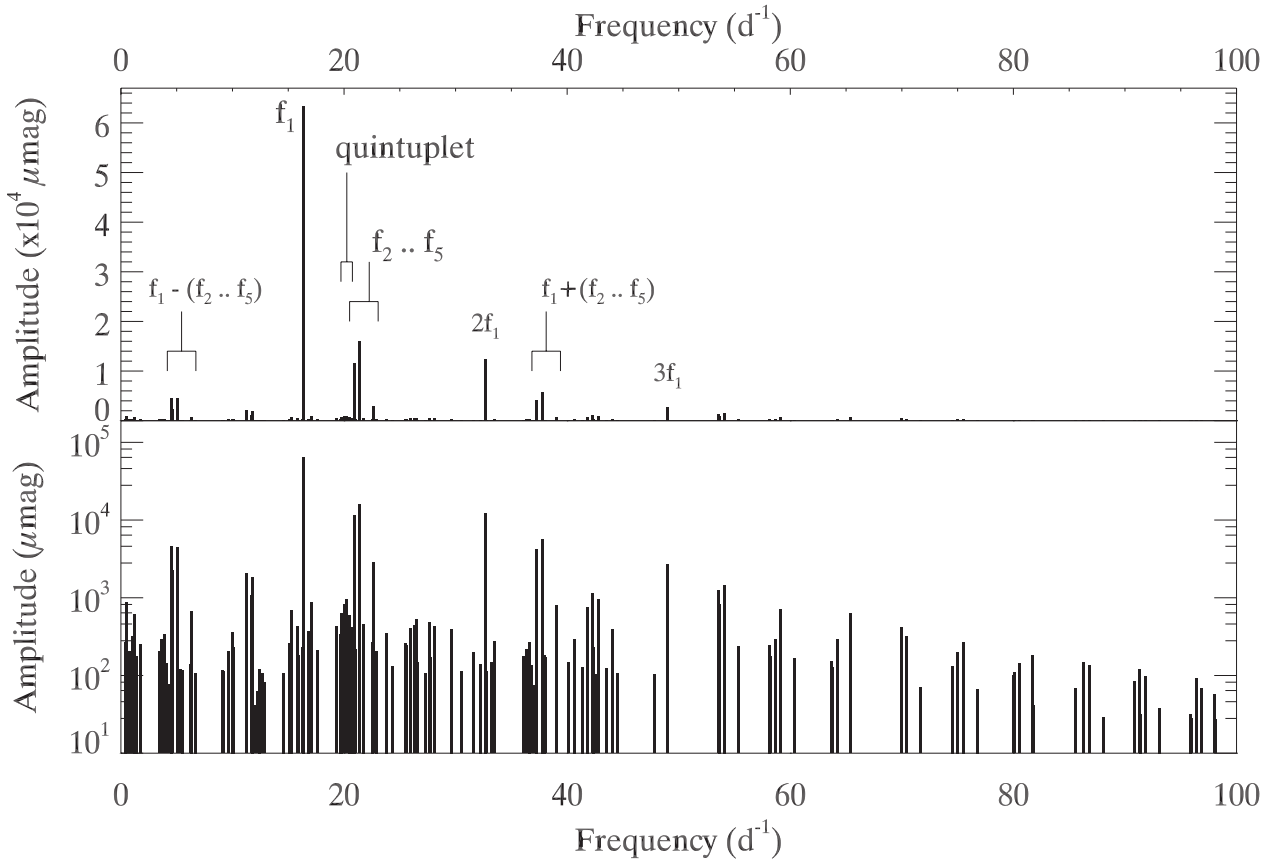


Figure 4. Upper panel: the schematic amplitude spectrum of KIC 11754974 from 0 to 100 d^{-1} . f_1-f_5 are the five highest amplitude peaks in the frequency region $16 < f < 25$, assigned in decreasing amplitude order. This region is magnified in Fig. 5. The $10^4\text{ }\mu\text{mag}$ peak at 32.7 d^{-1} is $2f_1$. Also labelled are the quintuplet (Section 4.4) and some combination frequencies (Section 4.5). f_4 is very close in frequency to f_3 ; the two are unresolvable in this figure, but f_4 has a higher frequency and the frequencies are resolved in the data. Lower panel: logarithmic version of the same plot. Note that these schematic diagrams show the frequencies listed in Table 4 only.

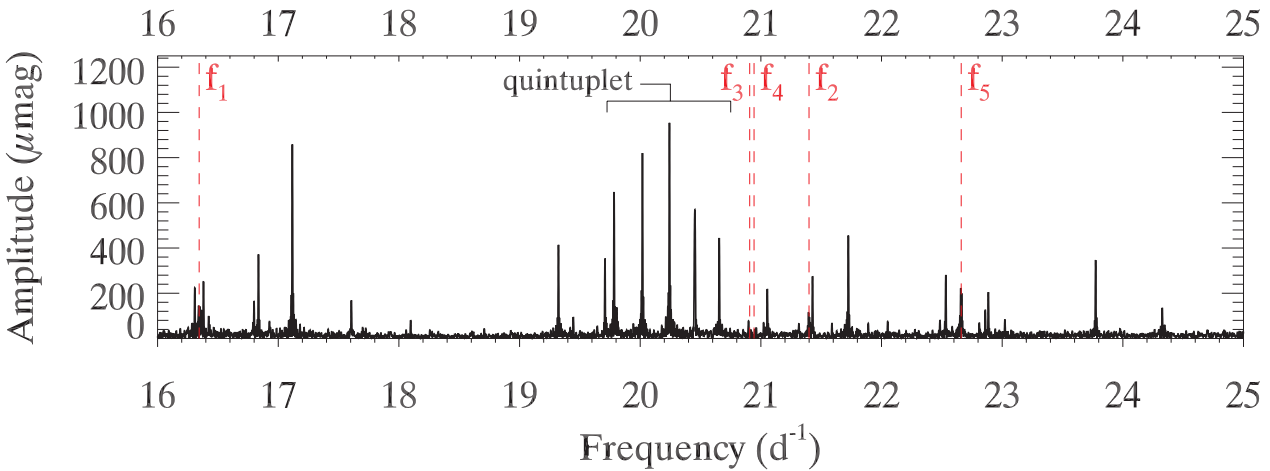


Figure 5. The amplitude spectrum of the combined Q6 and Q7 data set from 16 to 25 d^{-1} with f_1-f_5 pre-whitened. Without large amplitude modes dominating the scale, the large number of lower amplitude peaks becomes clear. The quintuplet centred at 20.243 d^{-1} is recognizable from its roughly equal spacings.

width of a peak at half-maximum (FWHM) is 0.0067 d . A stricter tolerance reduces the probability of false positives for frequency combinations, and has been made necessary because of the high number of frequencies extracted.

In addition to meeting the tolerance criterion, the combination must also be physically sensible – high coefficients and many

combining independent frequencies require increasingly unlikely interactions between modes. Hence, both the coefficients of the independent frequencies and the number of independent frequencies must be small. Sensible combinations typically have neither of those numbers greater than three, but no hard-and-fast rule was applied. In the region above 70 d^{-1} , the coefficients have to be quite

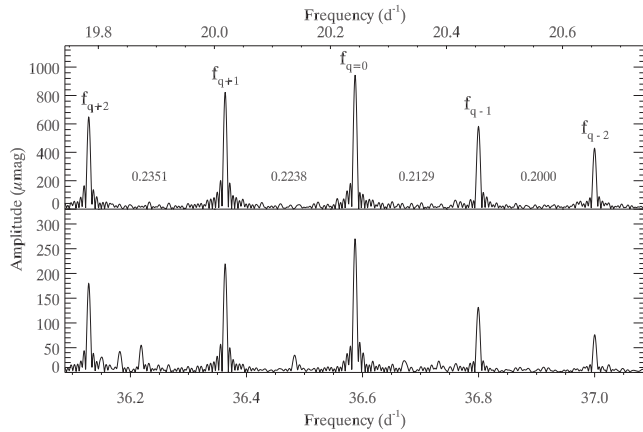


Figure 6. The main quintuplet at 20.242 d^{-1} (upper panel) and the quintuplet formed in combination with f_1 at 36.587 d^{-1} (lower panel). The spacings in the upper panel are equal to those in the lower one because the frequencies are formed in exact combinations with f_1 (but are only forced to be exact in the fitting – here, we present them as they are observed). Subscripted numbers represent the m -values of the mode. Least-squares uncertainties on the frequencies are $< 10^{-4} \text{ d}^{-1}$ in the bottom panel and $\ll 10^{-4} \text{ d}^{-1}$ in the top panel.

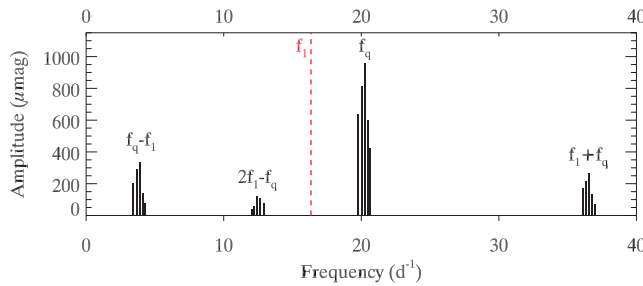


Figure 7. Schematic diagram of the many quintuplets in the data. The main quintuplet at 20.242 d^{-1} forms other quintuplets throughout the Fourier spectrum in combination with f_1 . One can see the similar amplitude ratios of the quintuplets as the shape of the quintuplet is maintained in each combination.

high, especially since f_1 is only 16.345 d^{-1} . We note that some of the remaining ‘independent’ frequencies without identifications in Table 4 can be explained with physically sensible combination frequencies if the tolerance is relaxed.

PERIOD04 is capable of testing for frequency combinations to a given tolerance criterion; such a method was employed by Breger et al. (2005) in their analysis of the star FG Vir, where their tolerance criterion was 0.001 d^{-1} . We used the same tolerance criterion and ran simulations to determine the number of accidentally matched frequencies one can expect. Using the frequencies f_1-f_5 , allowing coefficients between -1 and 6 , and allowing all five frequencies to be involved in the combinations simultaneously (i.e. there is much more freedom than in the combinations in Table 4), we find only one to two frequencies in the range $70-100 \text{ d}^{-1}$ to be accidentally matched. Hence, almost all combinations presented in Table 4 are probably genuine. The two frequencies with the greatest uncertainties lie at 91.377 and 95.939 d^{-1} , with errors of 0.001 d^{-1} , which is the same variation as the combination frequency tolerance. These are the lowest amplitude frequencies extracted, and are the two prime candidates for mismatched frequencies.

Combination frequencies are even detected at beyond 100 d^{-1} (not shown). Particular caution has been made in identifying high

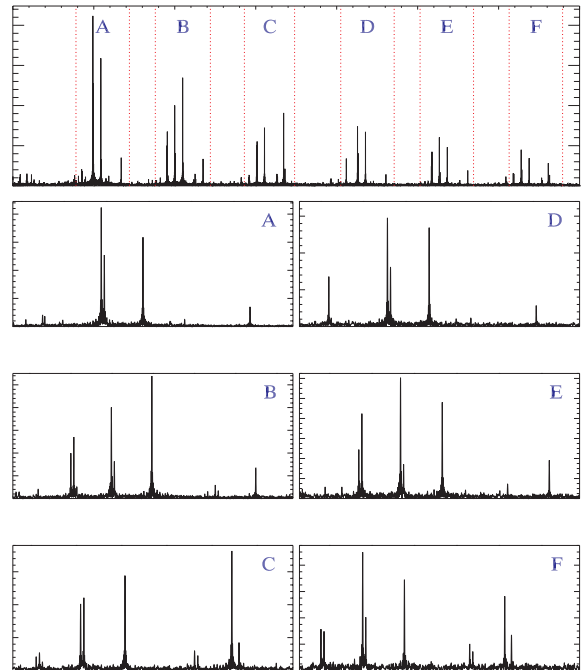


Figure 8. Repetitive patterns are caused by adding f_1 to other combinations of frequencies, hence panels A and D, B and E, and C and F are each separated in frequency by $f_1 = 16.345 \text{ d}^{-1}$. The frequency range displayed by each is shown in the top panel. The first peak in panel D is $4f_2$; $4f_2 - f_1$ is too low in amplitude to be distinguishable from noise; hence, it is not seen in panel A. The cause of relative amplitude changes of neighbouring peaks following the addition of f_1 is unclear, but the absolute changes in amplitudes in adjacent panels (note the change in axis scale – units are μmag) are a result of having a greater number of combination terms.

frequencies as combinations, especially because they often contain more than two independent frequencies and coefficients of 3 , 4 or even higher. There is no doubt, however, that these are indeed combinations. Several patterns of frequencies repeat themselves, separated by f_1 (Fig. 8), in a way that could only happen independently. The frequencies of these peaks are entirely calculable given the frequencies of the main independent modes, and at yet higher frequencies they recur with diminishing amplitudes until $\sim 140 \text{ d}^{-1}$ at which point their amplitudes become indistinguishable from noise and the patterns become less discernible when peaks are missing.

4.6 Validity of extracted frequencies

One could continue to extract frequencies down to lower and lower amplitudes, but this begs the question of where to stop. $100 \mu\text{mag}$ was chosen as a sensible limit, to extract the important frequencies for mode identification, and also for clarity: mode splittings become harder and harder to spot when the density of peaks increases, as happens when one lowers the extraction limit. On occasion, combination frequencies with amplitudes below $100 \mu\text{mag}$ were extracted, such as when they are expected as part of a multiplet. There are additional complications to extracting frequencies to lower amplitudes. With a 180 -d data set, frequency resolution is 0.006 d^{-1} . One cannot extract frequencies more closely spaced than this. Moreover, nothing is gained by continuing extraction to lower

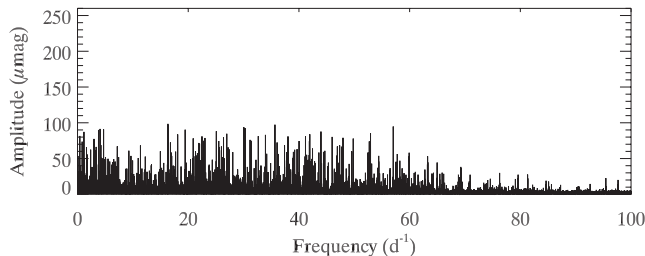


Figure 9. Residuals left behind after extraction of 166 frequencies, to amplitude limits $100 \mu\text{mag}$ for $0 \leq f \leq 70 \text{ d}^{-1}$, and $20 \mu\text{mag}$ for $70 < f \leq 100 \text{ d}^{-1}$.

amplitudes – combination frequencies become less reliable as the risk of false positives rises sharply with the number of extracted frequencies, mode identification becomes more difficult when mode density increases, and the low-amplitude frequencies become ‘noise’ interspersed with the meaningful high-amplitude peaks. Fig. 9 shows the residuals left after pre-whitening all frequencies in Table 4.

The Kepler Input Catalogue (KIC; Brown et al. 2011) provides information on the amount of light contamination appearing in the data. The value of contamination for KIC 11754974 is 0.009; hence, less than 1 per cent of light incident on the CCD pixels attributed to this star can be coming from background stars. As far as we can tell from looking at *Kepler* Full-Frame Images, 2MASS and DSS images, KIC 11754974 is safe from contamination. This makes negligible the possibility that a background star has a high-amplitude pulsation mode that is picked up and interpreted as a pulsation mode for KIC 11754974. We know that the star is in a binary system, but with a star significantly less massive than the Sun, contributing little light and not expected to generate frequencies in the periodogram at the amplitudes and frequencies observed.

It may be possible to check whether a frequency is a part of a combination or is an independent frequency by examining the relationship between phase and frequency for the combination terms. In a recent paper on KIC 9700322, in which many combination frequencies were detected, Breger et al. (2011) found that the higher frequency modes have greater relative phases. The theory is based on that developed by Buchler et al. (1997) who described non-linear resonances mathematically, and Balona (2012) investigated further. A combination term with frequency $f = n_i f_i + n_j f_j$ should have a relative phase, $\phi_r = \phi_c - (n_i \phi_i + n_j \phi_j)$, where ϕ_c is the phase calculated by least-squares fitting. We find that ϕ_r decreases with frequency once phase folding about 2π is taken into account – we shifted groups of points by multiples of 2π in phase until they lay roughly in a straight line, then made 2π corrections for individual points lying more than π away from the fit in an iterative way. All combination frequencies listed in Table 4 are plotted in Fig. 10. Those ‘combination frequencies’ that do not fit the correlation between ϕ_r and frequency in the figure might actually be independent frequencies, instead. On the other hand, perhaps the relationship is a purely mathematical construct. The points lying furthest from the fit are $3f_2$ and $4f_2$, which given the nature of the other combination frequencies in Table 4 would be expected to be present and with high S/N.

The correlation has been discussed by Balona (2012), who showed that for two interacting modes the phases of the harmonics of a given mode decrease linearly with increasing harmonic order (i.e. frequency). The observational evidence was not discussed in light of the precision with which frequencies, amplitudes and phases

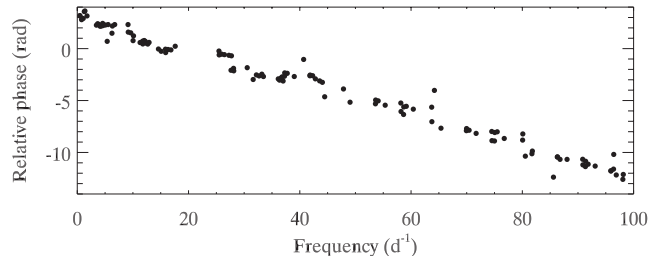


Figure 10. Relative phases are negatively correlated with frequency for the combination frequencies. Those points located far from the others might be interpreted as independent frequencies instead of combinations. Error bars for phases are shown, but are generally much smaller than the plot symbols. Phases and errors are the formal least-squares values and were calculated with respect to the mid-point of the combined Q6 and Q7 SC data set: $\text{BJD}_{\text{UTC}} 245\,5462.497\,92$.

can be determined with continuous space-based observations. The effect of such small error bars is to reduce the significance of the observational evidence substantially – the point with the median deviation lies over 27σ away from the fit. The median was chosen because taking the mean is biased towards those points with minuscule relative phase errors, whose distance from the fit can be many hundred σ . The combinations giving rise to such small errors typically involve f_1 and f_2 , the calculated phase errors of which are as low as 10^{-4} rad. This further supports a rejection of the hypothesis of any meaningful correlation, because combinations like $f_1 + f_2$ are superiorly statistically significant in terms of S/N, and should consequently lend greater weight in this correlation. The reduced chi-squared parameter, χ^2_{red} , is of the order of 10^5 , clearly indicating an inappropriate fit.

To establish whether the correlation need be rejected entirely, we ran a calculation whereby the frequency combinations and their phase errors were kept fixed, but instead of calculating phases from least squares we randomized them. We found that a correlation cannot be constructed by adding $\pm n2\pi$ to the random phases, so while it is clear that in the relative phases and frequencies of KIC 11754974 some correlation does exist, we conclude the correlation is neither tight nor useful.

5 ASTEROSEISMIC MODELS

KIC 11754974 lies near the red edge of the δ Sct instability strip. At these cooler temperatures, convection plays an important role. Indeed, without time-dependent convection (TDC) treatments, an actual red edge is not accurately predicted. Thus, the introduction of TDC models was an important step forward in the modelling of δ Sct stars (Dupret et al. 2004, 2005). Murphy et al. (2012) gave a successful first application of these models to an individual δ Sct star observed by *Kepler*.

Rotation plays a big role in the evolution and oscillations of δ Sct stars (Goupil et al. 2005; Rodríguez et al. 2006a,b; Poretti et al. 2011), even for KIC 11754974, which rotates slowly compared to the distribution of δ Sct star rotational velocities. Furthermore, asteroseismic analyses with rotating models can assist with mode identification through the effects of rotation on the mode couplings and frequency relationships (Suárez, Garrido & Goupil 2006a; Suárez, Garrido & Moya 2007).

No combination of both TDC and rotating models exists at present, so our modelling approach consists of the two methods applied separately. This section explains the details of the models used, and the methodology followed.

5.1 Description of the models

Our TDC models use the same tools and selection method as that explained in detail in Murphy et al. (2012); the codes used are the Code Liégeois d'évolution stellaire (Scuflaire et al. 2008) for structure models and the MAD code (Dupret 2001) supplemented with Gabriel's treatment of TDC (Gabriel 1996; Grigahcène et al. 2005) for non-adiabatic non-radial oscillation calculations. Convection was treated using mixing-length theory (MLT; Böhm-Vitense 1958), and TDC runs throughout the evolution calculations.

In order to theoretically characterize KIC 11754974, *pseudo-rotating* seismic models (see Soufi, Goupil & Dziembowski 1998; Suárez et al. 2002) of the star were built. These equilibrium models were computed with the evolutionary code CESAM (Morel 1997) using frozen convection (FC) and taking the strongest effects of rotation into account. The latter is done by including the spherically averaged contribution of the centrifugal acceleration, which is included by means of an effective gravity $g_{\text{eff}} = g - \mathcal{A}_c(r)$, where g is the local gravity, r is the radius and $\mathcal{A}_c(r) = \frac{2}{3}r\Omega^2(r)$ is the centrifugal acceleration of matter elements. The non-spherical components of the centrifugal acceleration are included in the adiabatic oscillation computations, but not in the equilibrium models (details in Suárez, Goupil & Morel 2006b).

Since we have no information about the internal rotation profile of KIC 11754974, i.e. about how the angular momentum is distributed in its interior, we have adopted the hypothesis of differential rotation caused by local conservation of the angular momentum (in the radiative zones) during the evolution of the star. Similar rotation profiles have been found when analysing the evolution of giant stars including rotationally induced mixing of chemical elements and transport of angular momentum (Maeder & Meynet 2004). The physics of the equilibrium models has been chosen as adequate for intermediate-mass A–F stars, and was described in detail by Suárez et al. (2009).

Adiabatic oscillations were computed using the adiabatic oscillation code FILOU (Suárez 2002; Suárez & Goupil 2008). This code provides theoretical adiabatic oscillations of a given equilibrium model corrected up to second order for the effects of rotation. These include near-degeneracy effects (mode coupling effects), which occur when two or more frequencies are close to each other. In addition, the perturbative description adopted takes radial variation of the angular velocity (differential rotation) into account in the oscillation equations. The oscillation spectra were calculated from frequencies around the fundamental radial mode (for each model) and the cut-off frequency. This allows the presence of low-order g and p modes (mixed modes), which are generally present in δ Sct stars. Since non-radial oscillations are expected, modes were computed from degrees $\ell = 0$ (radial) to $\ell = 3$. Although the calculations are adiabatic, the effects of rotation alter the frequencies by an amount greater than the use of non-adiabatic codes.

5.2 Methodology

The low T_{eff} of the target suggested TDC models would provide a more accurate first approach to the global properties of the star.

Table 5. Properties of the best TDC model, obtained by perturbing the spectroscopic parameters and convection efficiency.

Mass (M _⊕)	Radius (R _⊕)	T _{eff} (K)	Age (Myr)	log g (cgs)	log(L/L _⊕)	X	Z	α _{MLT}	d _{ov}
1.56	2.425	7110	1829	3.862	1.130	0.7465	0.0071	2.0	0.2

We selected the best-fitting model by perturbing the atmospheric parameters from Section 3 (Table 3) to obtain the best match with the observed oscillation frequencies, adjusting the TDC parameters (namely the convection efficiency) accordingly. The properties of the best TDC model are presented in Table 5.

It is important to stress that the TDC models do not include rotation. Our next step was therefore to calculate equivalent (in terms of global parameters) FC models, incorporating rotation. We considered that the error committed this way (i.e. TDC first) is much lower than through direct modelling with FC and rotation.

The modelling with rotating models involves building a grid, with masses ranging from 1.4 to 2.0 M_⊕ in steps of 0.1 M_⊕, a convective efficiency ranging from 0.5 (prescribed by Casas et al. 2006 for A–F stars) to 2.0 (which gave the best fit in TDC calculations) in steps of 0.1, and an overshoot parameter d_{ov} in the range of [0, 0.3] in steps of 0.05. The surface rotational velocity of the models, v_{eq} , ranged between 20 and 30 km s⁻¹ offering enough dispersion to analyse different configurations of mass, metallicity and age. In principle, this gives splittings close to those observed for the quintuplet, but this was not constrained to be the case. In addition, it indirectly guarantees a dispersion in the inclination angle probed within the model grid. Metallicity was limited to [Fe/H] = −0.5 ± 0.1 dex, though metallicities closer to the solar values were investigated and offered a poorer match with the observed frequencies. This implies that the entire star is metal poor, and that we are not just observing a surface abundance anomaly, thus arguing against a λ Boo classification (cf. debates in the literature about the interior metallicity of λ Boo stars, e.g. Moya et al. 2010).

Model selection involves searching through the grid, minimizing the mean-square error function χ^2 . For each mode,

$$\chi^2 = \frac{1}{N} \sum_{i=1}^N (f_{\text{obs},i} - v_{\text{th},i})^2 \quad (1)$$

is calculated, where $f_{\text{obs},i}$ and $v_{\text{th},i}$ represent the observed and theoretical frequencies respectively. The total number of observed frequencies is represented by N . Calculations are made considering the mass M , the rotational velocity v_{eq} , metallicity, α_{MLT} , d_{ov} and age as free parameters; pulsation amplitude information is not directly used. Importantly, all the frequencies are fitted simultaneously; assumptions like the ‘strongest modes’ being radial or quintuplet membership were not used as constraints for the models.

We did look separately for diagnostic frequency ratios in the data. We took models of three different masses and searched for ratios of 0.772 ± 0.009 (cf. discussion in Section 4.3) among the independent modes. Fig. 11 displays the four possible frequency ratios observed, none of which satisfies the T_{eff} and (rather loose) log g uncertainties, or indicates a particularly promising identification for the first radial overtone. We stress this only reduces the likelihood that $F1$ is present with $F1$; either could still be present without the other.

5.3 Discussion of the models

In general, we found that the models with the lowest χ^2 were below 1.60 M_⊕. Moreover, those that matched either $F1$ or $F1$ to

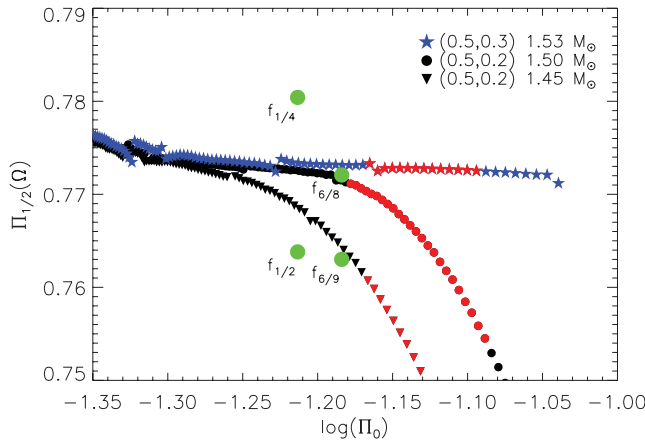


Figure 11. Rotational Petersen diagram covering models with $1.45\text{--}1.60 M_{\odot}$. Coloured in red are the models that satisfy the T_{eff} and $\log g$ uncertainties ($7000 \pm 200 \text{ K}$; 3.6 ± 0.5); we used a conservative $\log g$ uncertainty, because atmosphere models do not include rotation to calculate an effective gravity. Also plotted (green dots) are frequency ratios (e.g. $f_{1/4}$ indicates f_1/f_4) that fall within 0.772 ± 0.009 (see the text). Numbers in brackets in the legend denote the value of α_{MLT} and the overshooting parameter, respectively.

the observed frequencies had masses in the range $1.50\text{--}1.53 M_{\odot}$, which are very similar to the TDC-predicted masses. The best-fitting rotating model identifies f_1 as the fundamental radial mode, and the quintuplet as components of a mixed $(n, \ell) = (-1, 3)$ mode. The parameters of this model are displayed in Table 6.

That the quintuplet is identified as a mixed mode has strong implications. It directly affects the Ledoux constant, C_L , depending on how much g-mode character such a mode has. For lower radial orders, C_L can exceed 0.1 for $\ell = 2$ modes. Therefore, we had to search a range of low frequencies to account for this factor in Section 4.4, but still no peak due to rotation was found up to twice the expected value (i.e. between 0.218 and 0.436 d^{-1}).

The asymmetry of the quintuplet gives a proportionality constant, D_L , for the second-order effect (centrifugal force) of rotational splitting, which we can use as a consistency check. For moderately rotating δ Sct stars, oscillations can be expressed in terms of the perturbation theory as

$$\omega = \omega_0 + (C_L - 1)m\Omega + D_L \frac{m^2\Omega^2}{\omega_0},$$

which describes the effects of rotation up to second order (adapted from Dziembowski & Goode 1992), for a rotation frequency, Ω , and observed and intrinsic (unperturbed) pulsation frequencies, ω and ω_0 , respectively. Under the assumption that the quintuplet is actually an $\ell = 2$ mode, one gets $D_L = 2.45$ in the case of $C_L = 0$, or $D_L = 1.8$ for $C_L = 0.12$. These are about the expected values for an $(n, \ell) = (2, 2)$ mode. (See Dziembowski & Goode 1992 for

the example values.) The Q-value of an $(n, \ell) = (2, 2)$ mode at the observed quintuplet frequencies is consistent with the assumption that the lowest independent frequency is near the radial fundamental mode.

Thus, we have the following scenario: the best rotating model indicates that f_1 is the fundamental radial mode, and inferences on the Q-value of the quintuplet if it is an $(n, \ell) = (2, 2)$ mode, would agree with that identification for f_1 . However, the model predicts that the quintuplet is part of an $\ell = 3$ mode instead. This is only an apparent disagreement. First, that an $(n, \ell) = (2, 2)$ mode can generate the observed frequency quintuplet does not make its identification as part of an $\ell = 3$ septuplet impossible, as the expected rotational splitting asymmetry of such a mode is expected to be quite similar. Secondly, differential rotation in the radial direction is another possible explanation. It has been proven that the oscillations of low-order p and g modes are highly sensitive to variations of the rotation profile near the core (Suárez et al. 2006a). Further attempts at direct mode identification, through multicolour photometry, and further constraints for the models from high-S/N, high-resolution spectroscopy are required for further investigation.

6 CONCLUSIONS

KIC 11754974 is a cool, high-amplitude δ Sct star with a large number of combination frequencies that show a predictable pattern at high frequency. We discovered from the pulsations that the star is in a 343-d binary system; our seismic models show the primary (pulsating) member is $1.53 M_{\odot}$, making the secondary $0.63 M_{\odot}$ for a model-determined $i = 47^\circ$. No direct contribution from the secondary is seen in the spectrum or the light curve.

Compared to most A-type stars, KIC 11754974 is a slow rotator, which is typical of HADS stars, and allowed us to construct perturbative rotating models. The models indicate the star is metal poor, in that solar-metallicity models were a poor fit to the observed frequencies. This agrees with literature classifications that this is a Population II (SX Phe) star, and argues against a surface abundance anomaly model like the Am stars or λ Boo stars.

The location of this star on the rotating Petersen diagram argues against more than one of the high-amplitude f_1, \dots, f_5 modes being radial. We cannot confirm whether the quintuplet found in the data is rotationally split – direct mode identification is required for this.

Combination frequencies are present all across the spectrum, arising from five independent modes that are all confined to a small frequency region. Outside the frequency region $16 < f < 25 \text{ d}^{-1}$ independent modes with amplitudes above $500 \mu\text{mag}$ are non-existent, and most frequencies are combinations of some form.

The star has a lot of asteroseismic potential, being near the red-edge of the δ Sct instability strip where the pulsation–convection interaction is under study, being a Population II star with precise and sensitive photometry, and being a high-amplitude pulsator for which mode interaction is also particularly important. Here, we have

Table 6. Characteristics of the best representative rotating model. The first six columns have their usual meanings, then headings are mean density, equatorial rotation velocity, the ratio of the equatorial rotation velocity to the keplerian orbital velocity at the stellar surface, inclination of the stellar rotation axis to the line of sight, fundamental radial mode frequency $f(F1)$, first overtone radial mode frequency $f(F1)$, the base-10 logarithm of the period of $F1$, and the period ratio of $F1$ and $F1$. The model has metallicity $[\text{Fe}/\text{H}] = -0.52$, convective efficiency, $\alpha_{\text{MLT}} = 0.5$ and overshooting $d_{\text{ov}} = 0.3$. See Section 5.2 for model selection criteria.

Mass (M_{\odot})	Radius (R_{\odot})	T_{eff} (K)	Age (Myr)	$\log g$ (cgs)	$\bar{\rho}$	v_{eq} (km s^{-1})	i (deg)	$f(F1)$ (d^{-1})	$f(F1)$ (d^{-1})	$\log P(F1)$	$P(F1)/P(F1)$
1.53	1.764	7256	1465.93	4.129	0.392	34.18	47^{+7}_{-15}	16.327	21.1	-1.213	0.773

scratched the surface with our models, but there is great potential to learn much more. We intend to study the star further, with multicolour photometry and higher resolution spectroscopy to identify the pulsation modes and constrain the atmospheric parameters. Despite being faint, the star is a promising target for learning about mode selection in these pulsators.

ACKNOWLEDGEMENTS

This paper includes data collected by the *Kepler* mission. Funding for the *Kepler* mission is provided by the NASA Science Mission Directorate. The paper also includes observations made with the NOT, operated jointly by Denmark, Finland, Iceland, Norway and Sweden, on the island of La Palma at the Spanish Observatorio del Roque de los Muchachos of the Instituto de Astrofísica de Canarias (IAC). SJM would like to acknowledge the financial support of the STFC, and from the projects FCOMP-01-0124-FEDER-009292 and PTDC/CTE-AST/098754/2008 under grant CAUP-09/2012-BI. AP acknowledges the support from the NCN grant No. 2011/03/B/ST9/02667. Some calculations have been carried out in Wrocław Centre for Networking and Supercomputing (<http://www.wcss.wroc.pl>), grant No. 219. JCS acknowledges support by Spanish National Research Plan through grants ESP2010-20982-C02-01 and AYA2010-12030-E. KU acknowledges financial support by the Spanish National Plan of R&D for 2010, project AYA2010-17803. RS was supported by the János Bolyai Research Scholarship, the ‘Lendület-2009 Young Researchers’ Programme of the Hungarian Academy of Sciences, the HUMAN MB08C 81013 grant of the MAG Zrt, the Hungarian OTKA grant K83790 and the European Community’s Seventh Framework Programme (FP7/2007-2013) under grant agreement no. 269194 (IRSES/ASK). AOT acknowledges support from Sonderforschungsbereich SFB 881 ‘The Milky Way System’ (subproject A5) of the German Research Foundation (DFG). GH is thankful for support by the NCN grant 2011/01/B/ST9/05448.

REFERENCES

- Anders E., Grevesse N., 1989, *Geochim. Cosmochim. Acta*, 53, 197
 Balona L. A., 2011, *MNRAS*, 415, 1691
 Balona L. A., 2012, *MNRAS*, 422, 1092
 Balona L. A., Nemec J. M., 2012, *MNRAS*, 426, 2413
 Balona L. A., Guzik J. A., Uytterhoeven K., Smith J. C., Tenenbaum P., Twicken J. D., 2011, *MNRAS*, 415, 3531
 Blackwell D. E., Shallis M. J., 1977, *MNRAS*, 180, 177
 Böhm-Vitense E., 1958, *Z. Astrophys.*, 46, 108
 Breger M., Bregman J. N., 1975, *ApJ*, 200, 343
 Breger M. et al., 2005, *A&A*, 435, 955
 Breger M., Davis K. A., Dukes R. J., 2008, *Commun. Asteroseismol.*, 153, 63
 Breger M. et al., 2011, *MNRAS*, 414, 1721
 Brown T. M., Latham D. W., Everett M. E., Esquerdo G. A., 2011, *AJ*, 142, 112
 Buchler J. R., Goupil M., Hansen C. J., 1997, *A&A*, 321, 159
 Casas R., Suárez J. C., Moya A., Garrido R., 2006, *A&A*, 455, 1019
 Castanheira B. G., Breger M., Beck P. G., Elmasli A., Lenz P., Falcon R. E., 2008, *Commun. Asteroseismol.*, 157, 124
 Dupret M. A., 2001, *A&A*, 366, 166
 Dupret M.-A., Grigahcène A., Garrido R., Gabriel M., Scuflaire R., 2004, *A&A*, 414, L17
 Dupret M.-A., Grigahcène A., Garrido R., De Ridder J., Scuflaire R., Gabriel M., 2005, *MNRAS*, 361, 476
 Dziembowski W. A., Goode P. R., 1992, *ApJ*, 394, 670
 Eastman J., Siverd R., Gaudi B. S., 2010, *PASP*, 122, 935
 Gabriel M., 1996, *Bull. Astron. Soc. India*, 24, 233
 Goupil M.-J., Dupret M. A., Samadi R., Boehm T., Alecian E., Suárez J. C., Lebreton Y., Catala C., 2005, *JA&A*, 26, 249
 Grigahcène A., Dupret M.-A., Gabriel M., Garrido R., Scuflaire R., 2005, *A&A*, 434, 1055
 Guzik J. A., Breger M., 2011, *Commun. Asteroseismol.*, 162, 62
 Guzik J. A., Bradley P. A., Templeton M. R., 2000, in Breger M., Montgomery M., eds, *ASP Conf. Ser. Vol. 210, Delta Scuti and Related Stars*. Astron. Soc. Pac., San Francisco, p. 247
 Heiter U. et al., 2002, *A&A*, 392, 619
 Koch D. G. et al., 2010, *ApJ*, 713, L79
 Kupka F., Piskunov N., Ryabchikova T. A., Stempels H. C., Weiss W. W., 1999, *A&AS*, 138, 119
 Lenz P., Breger M., 2004, in Zverko J., Ziznovsky J., Adelman S. J., Weiss W. W., eds, *Proc. IAU Symp. 224, The A-Star Puzzle*. Cambridge Univ. Press, Cambridge, p. 786
 Lenz P., Breger M., 2005, *Commun. Asteroseismol.*, 146, 53
 Maeder A., Meynet G., 2004, in Maeder A., Eenens P., eds, *Proc. IAU Symp. 215, Stellar Rotation*. Astron. Soc. Pac., San Francisco, p. 500
 Morel P., 1997, *A&AS*, 124, 597
 Moya A., Amado P. J., Barrado D., Hernández A. G., Aberasturi M., Montesinos B., Aceituno F., 2010, *MNRAS*, 406, 566
 Murphy S. J., 2012a, *MNRAS*, 422, 665
 Murphy S. J., 2012b, *Astron. Nachr.*, 333, 1057
 Murphy S. J., Grigahcène A., Niemczura E., Kurtz D. W., Uytterhoeven K., 2012, *MNRAS*, 427, 1418
 Murphy S. J., Shibahashi H., Kurtz D. W., 2013, *MNRAS*, 430, 2986
 Nemec J., Mateo M., 1990, in Cacciari C., Clementini G., eds, *ASP Conf. Ser. Vol. 11, Confrontation Between Stellar Pulsation and Evolution*. Astron. Soc. Pac., San Francisco, p. 64
 Olech A., Dziembowski W. A., Pamyatnykh A. A., Kaluzny J., Pych W., Schwarzenberg-Czerny A., Thompson I. B., 2005, *MNRAS*, 363, 40
 Paunzen E., Iliev I. K., Kamp I., Barzova I. S., 2002, *MNRAS*, 336, 1030
 Paunzen E., Heiter U., Fraga L., Pintado O., 2012, *MNRAS*, 419, 3604
 Petersen J. O., 1978, *A&A*, 62, 205
 Petersen J. O., Christensen-Dalsgaard J., 1996, *A&A*, 312, 463
 Pigulski A., Pojmański G., Pilecki B., Szczygieł D. M., 2009, *Acta Astron.*, 59, 33
 Piskunov N. E., 1992, in Glagolevskij Y. V., Romanyuk I. I., eds, *Physics and Evolution of Stars: Stellar Magnetism*. Nauka, St. Petersburg, p. 92
 Pollacco D. L. et al., 2006, *PASP*, 118, 1407
 Poretti E., 2003, *A&A*, 409, 1031
 Poretti E. et al., 2011, *A&A*, 528, A147
 Rodríguez E. et al., 2006a, *A&A*, 450, 715
 Rodríguez E. et al., 2006b, *A&A*, 456, 261
 Scuflaire R., Théado S., Montalbán J., Miglio A., Bourge P.-O., Godart M., Thoul A., Noels A., 2008, *Ap&SS*, 316, 83
 Shibahashi H., Kurtz D. W., 2012, *MNRAS*, 422, 738
 Soufi F., Goupil M. J., Dziembowski W. A., 1998, *A&A*, 334, 911
 Suárez J. C., 2002, PhD thesis, Observatoire de Paris
 Suárez J. C., Goupil M. J., 2008, *Ap&SS*, 316, 155
 Suárez J. C., Garrido R., Goupil M. J., 2006a, *A&A*, 447, 649
 Suárez J. C., Goupil M. J., Morel P., 2006b, *A&A*, 449, 673
 Suárez J. C., Garrido R., Moya A., 2007, *A&A*, 474, 961
 Suárez J.-C., Michel E., Pérez Hernández F., Lebreton Y., Li Z. P., Fox Machado L., 2002, *A&A*, 390, 523
 Suárez J. C., Moya A., Amado P. J., Martín-Ruiz S., Rodríguez-López C., Garrido R., 2009, *ApJ*, 690, 1401
 Uytterhoeven K. et al., 2011, *A&A*, 534, A125
 Wu Y., 2001, *MNRAS*, 323, 248
 Zacharias N., Finch C. T., Girard T. M., Henden A., Bartlett J. L., Monet D. G., Zacharias M. I., 2012, *VizieR Online Data Catalog*, 1322, 0